



# Hierarchical leaf-shaped Ni@Zn bimetallic catalyst with high stability and selectivity for borohydride oxidation

Bihao Hu<sup>a</sup>, Peng Chen<sup>a</sup>, Chuanlan Xu<sup>a</sup>, Jiazhi Meng<sup>a</sup>, Jinliang Cai<sup>a</sup>, Ying Yang<sup>a</sup>, Biao Zhang<sup>a</sup>, Danmei Yu<sup>a,\*</sup>, Xiaoyuan Zhou<sup>b,\*</sup>, Changguo Chen<sup>a,\*</sup>

<sup>a</sup> School of Chemistry and Chemical Engineering, Chongqing University, Chongqing 401331, PR China

<sup>b</sup> College of Physics, Chongqing University, Chongqing 401331, PR China

## ARTICLE INFO

### Keywords:

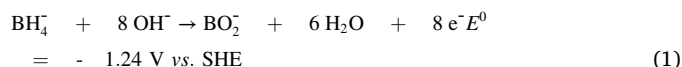
Borohydride oxidation reaction  
Hierarchical morphology  
Bimetal  
Nickel

## ABSTRACT

The bimetallic nickel zinc catalyst (Ni@Zn) with hierarchical morphology has been fabricated successfully by an ultrafast and simple synthesis strategy. Unique hierarchical morphology of the catalyst composes of honeycomb arrays, which are formed by Ni shell/Zn core leaves. This Ni@Zn possesses excellent catalytic activity, stability, and selectivity towards borohydride oxidation reaction (BOR). Moreover, a direct borohydride fuel cell (DBFC) with the Ni@Zn/C anode delivers a peak power density of 180.3 mW cm<sup>-2</sup> at 298 K. The outstanding performances originate from the increase of electroactive surface area, enhancement of reactants adsorption, and the inhibition of Ni oxidation, which are attributed to its unique hierarchical structure and the introduction of Zn. This study may provide important inspiration for developing efficient noble-metal-free catalysts for DBFC.

## 1. Introduction

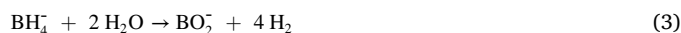
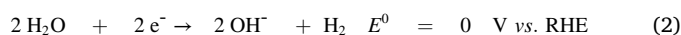
As an alkaline fuel cell, the direct borohydride fuel cell (DBFC) has been investigated since 1960 [1], fed usually with sodium borohydride (NaBH<sub>4</sub>) as a fuel [2]. The main advantages of NaBH<sub>4</sub> as a fuel are the complete eight-electron borohydride oxidation reaction (BOR, Eq. (1)) at a low electrode potential of -1.24 V vs. SHE and the large mass concentration of hydrogen (10.6 wt%) [3]. Therefore, when using O<sub>2</sub> as the oxidant, DBFC can obtain theoretically the open cell voltage of 1.64 V and the energy density of 9.30 kW h kg<sup>-1</sup> [4], but under the same condition, that of the proton exchange membrane fuel cell (PEMFC) is 1.23 V and 3.28 kW h kg<sup>-1</sup>, respectively [5].



DBFC is an eco-friendly energy source because no carbon cycle is involved and non-polluting product metaborate is regenerated potentially into NaBH<sub>4</sub> [6]. Moreover, NaBH<sub>4</sub> can exist steadily in a strongly alkaline environment [7], which is convenient for storage and transportation. When using hydrogen peroxide (H<sub>2</sub>O<sub>2</sub>) in an acidic medium, which has much a faster reduction process compared with O<sub>2</sub> as oxidation [8], DBFC can generate a much higher open cell voltage (ca.

2.18 V) [9] and energy density (17 kW h kg<sup>-1</sup>) [10]. So, this all-liquid DBFC shows prospective interest applications for mobile devices.

The platinum group metal (PGM), such as Pt and Pd, which have strong adsorption to BH<sub>4</sub><sup>-</sup> [11], is usually used as effective electrocatalysts for BOR. However, the non-negligible hydrogen evolution reaction (HER, Eq. (2)) [12] can be catalyzed efficiently by the Pt due to the low overpotential. The open cell voltage of DBFC decreases markedly in practice because HER competing with the expected BOR takes place mainly below anode potential of 0 V vs. RHE [13]. Another unfavored reaction competitive with BOR on Pt is the parallel non-faradaic heterogeneous hydrolysis of BH<sub>4</sub><sup>-</sup> (Eq. (3)) [5,14], which leads to the actual transfer electrons short of 8. Compared with Pt, Pd shows slightly lower catalytic activity to BOR [15] and lower HER activity [16], leading to a lower BOR onset potential [17]. However, the drawback that the hydrolysis of BH<sub>4</sub><sup>-</sup> still exists during BOR on Pd catalyst [18].



Non-noble materials, e.g., Ni and Co, are also catalytic active to BOR. It has been proven that Ni is a promising highly active material in DBFC because BOR has much lower onset potential and higher current density

\* Corresponding authors.

E-mail addresses: [yudanmei-1@163.com](mailto:yudanmei-1@163.com) (D. Yu), [xiaoyuan2013@cqu.edu.cn](mailto:xiaoyuan2013@cqu.edu.cn) (X. Zhou), [cgchen@cqu.edu.cn](mailto:cgchen@cqu.edu.cn) (C. Chen).

<https://doi.org/10.1016/j.apcatb.2022.121183>

Received 4 December 2021; Received in revised form 17 January 2022; Accepted 3 February 2022

Available online 4 February 2022

0926-3373/© 2022 Elsevier B.V. All rights reserved.

on Ni catalysts than that on PGM, especially at low overpotentials [12, 19,20]. However, the actual implementation of the Ni catalyst in DBFC is limited by two main impairments except for the maintaining grossly different pH at the anode and cathode in the fuel cell [9,19]. On the one hand, the surface state of Ni plays a decisive role because only metallic Ni performs relatively high activity towards the BOR [12]. But the strong alkaline environment required for the stable existence of  $\text{NaBH}_4$  prompts the oxidation of Ni, especially at high anode potentials, resulting in a sharp attenuation of activity to BOR [12]. On the other hand, as with PGM, Ni also demonstrates not bad catalytic activity to the HER during BOR as it has been used widely as catalysts for HER/hydrogen oxidation reaction (HOR) [21–23]. Moreover, the hydrolysis of  $\text{BH}_4^-$  is favored on the Ni and its alloys catalysts [24], leading to the decrease in fuel utilization of DBFC. As far as we know, there is not nearly the report that a noble-metal-free DBFC anode catalyst can satisfy the activity, stability, and selectivity at the same time.

On account of the potential synergy effect between multiple metals, alloying is recognized to be an effective way to fabricate efficient heterogeneous catalysts via tuning the surface properties [25–29]. So high-activity PGM is often introduced into the non-noble metal to improve the overall catalytic activity to BOR [30]. Furthermore, the fabrication of multi-metal nanocatalysts is a promising proposal to lessen the use of precious metals while maximizing the electrochemically active area. However, it is rather difficult to synthesize multi-metal catalysts with specific structure and element distribution because of atomic homogeneous mixing induced by nanomaterials with the high entropy trait [31–33]. Also, the different physical or chemical nature of the metal components can cause spoilage for some metal phases during use, which seriously affects the catalyst stability [34]. Therefore, the design and preparation of multi-metal catalysts with optimal and suitable structures have always been a challenge. Compared with alloy strategy, the design of catalyst with core-shell structure is considered to be a more effective idea to improve the catalyst's performance, owing to large surface-to-volume ratios [35] and unique catalytic characteristics [36,37]. Core-shell catalysts were used as electrocatalysts in various electrocatalytic systems, including in the BOR. Different core-shell electrocatalysts have been fabricated to BOR in recent years, such as Ni@Au [38],  $\text{C}_{\text{Ni-Sp}}/\text{rGP1}$  [39], Ni@M (M = Ru, Pd, Pt) [40], and Cu@Ag [41]. Nevertheless, the main purpose of these core-shell catalysts is to decrease the loading of noble metal but not to realize no noble metal. As a result, it is necessary to develop a noble-metal-free multi-metal catalyst to achieve an all-win situation in terms of activity, stability, and selectivity.

Herein, we developed an innovation strategy to solve the above-mentioned problems by fabricating an efficient bimetallic Ni@Zn catalyst with hierarchical morphology toward BOR via a simple and rapid two-step electrodeposition method. This unique hierarchical morphology is composed of honeycomb arrays, which are formed by core-shell leaves. The hierarchical morphology maximizes the electrochemically active area, while the introduction of Zn strengthens the adsorption of reactants and inhibits the oxidation of Ni. Compared with other Ni-based catalysts, the Ni@Zn catalyst demonstrates much higher catalytic activity, stability, and selectivity.

## 2. Experiment

### 2.1. Materials and synthesis

$\text{NiCl}_2 \cdot 6\text{H}_2\text{O}$ ,  $\text{ZnCl}_2$ ,  $\text{NH}_4\text{Cl}$ ,  $\text{NaBH}_4$ , and NaOH were purchased from Chengdu Cologne Chemical Co. Ltd, China, and commercial Ni sheets (NS) were obtained from Guantai Metal Material Co. Ltd, China. All chemicals were used without further purification.

Commercial NS was used as substrates after polishing by 400 mesh sandpapers, immersing ultrasonically in ethanol and 30 wt% NaOH solution for 5 min, respectively, then ultrasonic cleaning with deionized water and drying in turn. Pre-processed NS was twined by the electrical

tape to ensure the reaction area of  $1\text{ cm} \times 1\text{ cm}$ .

Ni@Zn catalyst was prepared by two-step electrodeposition on a pre-processed NS substrate. The first electrodeposition is performed with a constant current of  $1\text{ A cm}^{-2}$  in  $0.035\text{ M ZnCl}_2$  and  $4.0\text{ M NH}_4\text{Cl}$  solution for 20 s at  $25^\circ\text{C}$ . Then the second electrodeposition was carried out with a constant current of  $0.5\text{ A cm}^{-2}$  in  $0.2\text{ M NiCl}_2$  and  $4.0\text{ M NH}_4\text{Cl}$  solution for 20 s at  $25^\circ\text{C}$ . The schematic diagram of the preparation process of Ni@Zn catalysts is exhibited in Fig. S1. Synthesis of Ni catalysts was performed by constant current electrodeposition at a current density of  $0.5\text{ A cm}^{-2}$  for 20 s in  $0.2\text{ M NiCl}_2$  and  $4.0\text{ M NH}_4\text{Cl}$  solution at  $25^\circ\text{C}$  using an NS substrate. NiZn catalyst was fabricated by the same method as that of Ni catalysts except the electrodeposition bath containing an additional  $0.035\text{ M ZnCl}_2$ . The pretreated NS was used as a commercial Ni catalyst.

### 2.2. Materials characterization

The morphology and structure of catalysts were measured by a field emission scanning electron microscope (FE-SEM, JSM-7800 F) and transmission electron microscopy (TEM, Talos 200). X-ray diffraction (XRD) patterns of catalysts were recorded by a Shimadzu XRD6000 diffractometer with  $\text{Cu K}\alpha$  radiation at 40 kV and 30 mA. The texture coefficient ( $TC_{\text{hkl}}$ ) can be used to quantitatively estimate the preferred orientation of crystal materials and it was calculated according to the following Eq. (4) [42]:

$$TC_{\text{hkl}} = \frac{\left[ \frac{I_{\text{hkl}}}{I_{0(\text{hkl})}} \right]}{\left[ \sum_{i=1}^n \left( \frac{I_{\text{hkl}}}{I_{0(\text{hkl})}} \right) \right]} \times 100\% \quad (4)$$

where  $I_{\text{hkl}}$  and  $I_{0(\text{hkl})}$  represent the diffraction intensity of samples and the standard powder given by the JCPDS data (PDF#04-0850), respectively, and  $n$  is the total number of diffraction peaks. If the value of  $TC$  is greater than  $1/n$ , the crystal plane is a preferred orientation plane. The X-ray photoelectron spectroscopy (XPS, Thermo Fisher Scientific ESCALAB250Xi, Al  $\text{K}\alpha$ ) was performed to explore the surface composition of catalysts, where the C 1s peak at 284.8 eV (i.e. the surface adventitious carbon) was used to be as the calibration peak.

### 2.3. Electrochemical measurements

Electrochemical measurements were carried out in a traditional three-electrode system with prepared catalysts as a working electrode, graphite stripe as a counter electrode, and Hg/HgO as a reference electrode ( $E_{\text{Hg/HgO}} = 0.924\text{ V}$  vs. RHE, pH = 14.3). All electrochemical tests were performed by the Chi660e instrument (Shanghai Chen Hua Instrument Co. Ltd.). Linear sweep voltammetry (LSV) and Cyclic voltammetry (CV) were measured with a scan rate of  $10\text{ mV s}^{-1}$ . Chronoamperometry (CA) tests were conducted at  $0.1\text{ V}$  vs. RHE. Electrochemical impedance spectroscopy (EIS) was performed in the range of  $10^{-2}\text{ Hz} \sim 100\text{ kHz}$  with a signal amplitude of  $5\text{ mV}$  around  $E = 0.1\text{ V}$  vs. RHE. The values of circuit elements were simulated according to equivalent circuits via ZSimpWin. NaOH solution ( $2.0\text{ M}$ ) with  $0.135\text{ M NaBH}_4$  and NaOH solution ( $2.0\text{ M}$ ) were employed as the electrolyte for BOR and HER, respectively. The electrochemical active surface area (ECSA) of catalysts was estimated by CV [12,43]. Briefly, CV curves in the potential range from  $-0.06$ – $0.60\text{ V}$  vs. RHE were performed, shown in Fig. S2. The ECSA of catalysts was calculated as follows Eq. (5) [12,43]:

$$\text{ECSA} = Q_A / 0.514 \quad (5)$$

where  $Q_A$  is the entire anodic charge of the CV curves. The value of activation energies ( $E_a$ ) of BOR on catalysts were evaluated by the Arrhenius equation (Eq. (6)) [44]:

$$\frac{\partial \ln j}{\partial \frac{1}{T}} = -\frac{E_a}{R} \quad (6)$$

where  $j$  ( $\text{mA cm}^{-2}$ ) is the current density of BOR measured at  $E = 0.3$  V vs. RHE,  $T$  (K) is the test temperature,  $E_a$  ( $\text{J mol}^{-1}$ ) is the activation energy,  $R$  is the gas constant ( $8.314 \text{ J mol}^{-1} \text{ K}^{-1}$ ). Fuel efficiency was measured by the LAND system with a constant current of  $10 \text{ mA cm}^{-2}$  and calculated as follows Eq. (7):

$$\eta = tI / nZF \quad (7)$$

where  $\eta$  stands for fuel efficiency,  $t$  is the discharge time,  $I$  is the constant current of  $10 \text{ mA cm}^{-2}$ ,  $n$  is the number of transfer electrons which is equal to 4 for Ni,  $Z$  is the amount of substance of  $\text{NaBH}_4$  and  $F$  is Faraday constant ( $94685 \text{ C mol}^{-1}$ ). To perform an accelerated durability test (ADT) on catalysts, the CV test was repeated 500 times in the potential range from 0 V to 0.2 V vs. RHE at a scan rate of  $100 \text{ mV s}^{-1}$  in 0.135 M  $\text{NaBH}_4$  and 2 M  $\text{NaOH}$  mixture solution.

A unit cell of DBFC is equipped with  $\text{Ni@Zn/C}$  as the anode, 1.0 M  $\text{NaBH}_4$  and 3.0 M  $\text{NaOH}$  mixture solution as anolyte, commercial 10%  $\text{Pt/C}$  as the cathode and 4.0 M  $\text{H}_2\text{O}_2$  and 1.0 M  $\text{H}_2\text{SO}_4$  mixture solution as catholyte, and Nafion 117 membrane as proton exchange membrane, the schematic diagram shown in Fig. S3. The LSV tests and performed with a scan rate of  $1 \text{ mV s}^{-1}$  in a potential range from OCP to 0 V. The specific process is described in the Supporting Information.

### 3. Results and discussion

#### 3.1. Morphology and structure of $\text{Ni@Zn}$

The  $\text{Ni@Zn}$  catalyst is fabricated via two-step electrodeposition (Fig. S1). Firstly, Zn is obtained using the pretreated NS substrate as cathode and graphite as anode, applying constant current in the electrodeposition solution of  $\text{ZnCl}_2$  and  $\text{NH}_4\text{Cl}$ . The cathode surface exhibits black after electrodeposition due to the formation of Zn (Fig. S4b). From Fig. 1a, it is found that the uniform dispersed leaf-shaped Zn forms a honeycomb array on the NS surface. Subsequently, with Zn as the cathode and graphite as the anode, constant current electrodeposition is carried out in the solution containing  $\text{NiCl}_2$  and  $\text{NH}_4\text{Cl}$ . The cathode surface turns light grey at the end of deposition (Fig. S4c), that is to say, the  $\text{Ni@Zn}$  catalyst is obtained. In Fig. 1b, the obvious morphology changes of the cathode surface can be seen. The honeycomb arrays formed by leaves still exist, but multilayer structures appear because of the leaves stacking. At the same time, the thickness of leaves increases

owing to the coverage layer emerging. It can be inferred that leaf-shaped Zn growing on the NS are used as the framework of  $\text{Ni@Zn}$  catalyst's formation during the second electrodeposition, while the deposition of Ni on the framework forms the leaf-shaped structure of the Zn core and Ni shell. Thus, the formation process of  $\text{Ni@Zn}$  could be schematized in Fig. 1c.

A transmission electron microscope (TEM) was used to further observe the core-shell structure of  $\text{Ni@Zn}$  leaf. From the high-angle annular dark-field (HAADF) image (Fig. 2a), the multilayer leaves morphology can be seen consistent with the SEM images. Corresponding energy-dispersive X-ray spectroscopy (EDS) element maps are shown in Fig. 2b-d. The dispersion of Zn and Ni element is even in  $\text{Ni@Zn}$  leaf, while the unique core-shell structure of  $\text{Ni@Zn}$  leaf can be vindicated by obvious encompassment of Ni element to Zn element, shown as Fig. 2d and Fig. S5b. Hence,  $\text{Ni@Zn}$  catalyst with unique hierarchical morphology is successfully synthesized by simple two-step electrodeposition. The primary structure is the micron-level honeycomb array. While the secondary structure is formed from stacking multilayer leaves that possess the structure of Zn core and Ni shell. Besides, Multilayer and jagged features of the leaf-shaped structure could be more conducive to exposure to the high-index facets with steps, kinks, and low-coordination numbers [45] and increase further the reactive sites of catalysts to BOR.

In addition, the X-ray diffraction (XRD) pattern (Fig. 2e) confirms the face-centered cubic crystalline structure of  $\text{Ni@Zn}$  with only three peaks  $44.4^\circ$ ,  $51.9^\circ$ , and  $76.5^\circ$ , corresponding to the (111), (200) and (220) crystal facets of Ni. It also suggests that the leaf-shaped framework is completely covered by metal Ni. Moreover,  $\text{Ni@Zn}$  does exhibit a high extent of preferred orientation of Ni (220) facet (Fig. 2f), as does the  $\text{NiZn}$ . Therefore, it can be speculated that the introduction of Zn may induce Ni to grow oriented along the (220) crystal facet. High-index facets normally can easily interact with reactants and serve as catalytically active centers, thus giving rise to an obvious improvement of catalytic activity. This ascribes to the existence of a high density of low-coordinated surface atoms on the high-index facets, which contributes to the bond breaking of reactants [45–47]. Besides the high surface energy of the high-index facets is favorable to the adsorption to reactants, and the capture and further oxidation of  $\text{H}_2$  generated by the hydrolysis of borohydride [45,48]. Consequently, the  $\text{Ni@Zn}$  may demonstrate a high catalytic activity, leading to the significant enhancement fuel efficiency of DBFC.

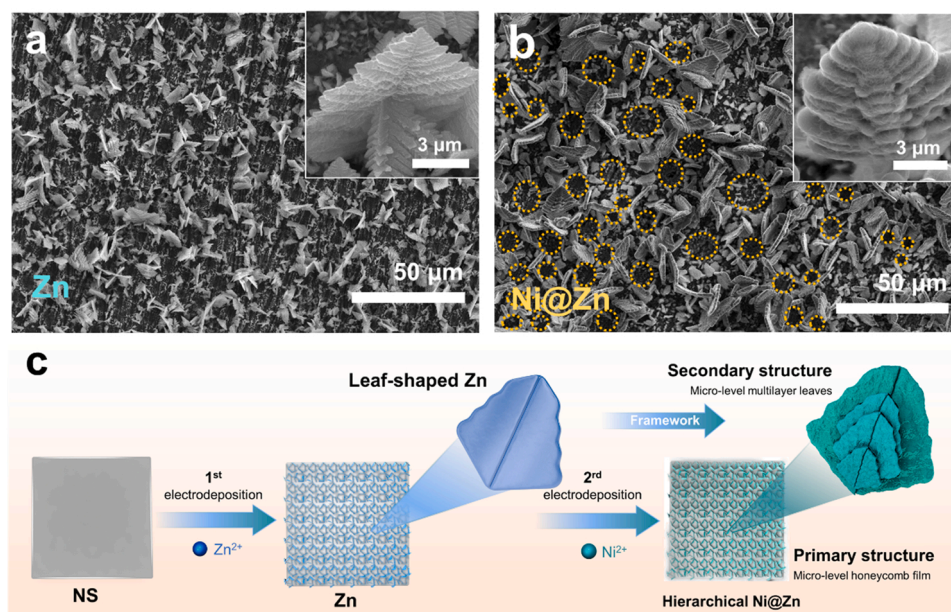


Fig. 1. SEM images of (a) Zn, (b)  $\text{Ni@Zn}$ ; (c) the schematic illustration of  $\text{Ni@Zn}$  formation.



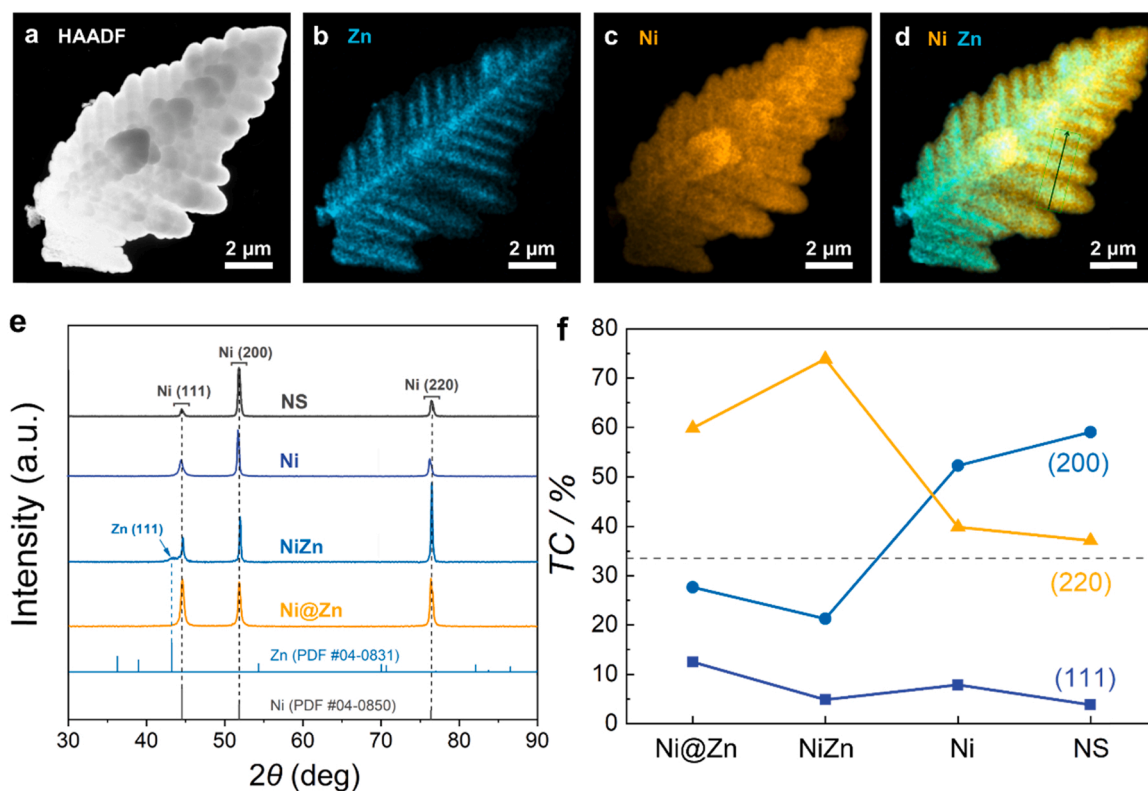


Fig. 2. (a) HAADF image of Ni@Zn catalyst and (b-d) corresponding EDS elemental maps; (e) XRD patterns and (f) the  $TC_{(hkl)}$  values of NS, Ni, NiZn, and Ni@Zn catalysts.

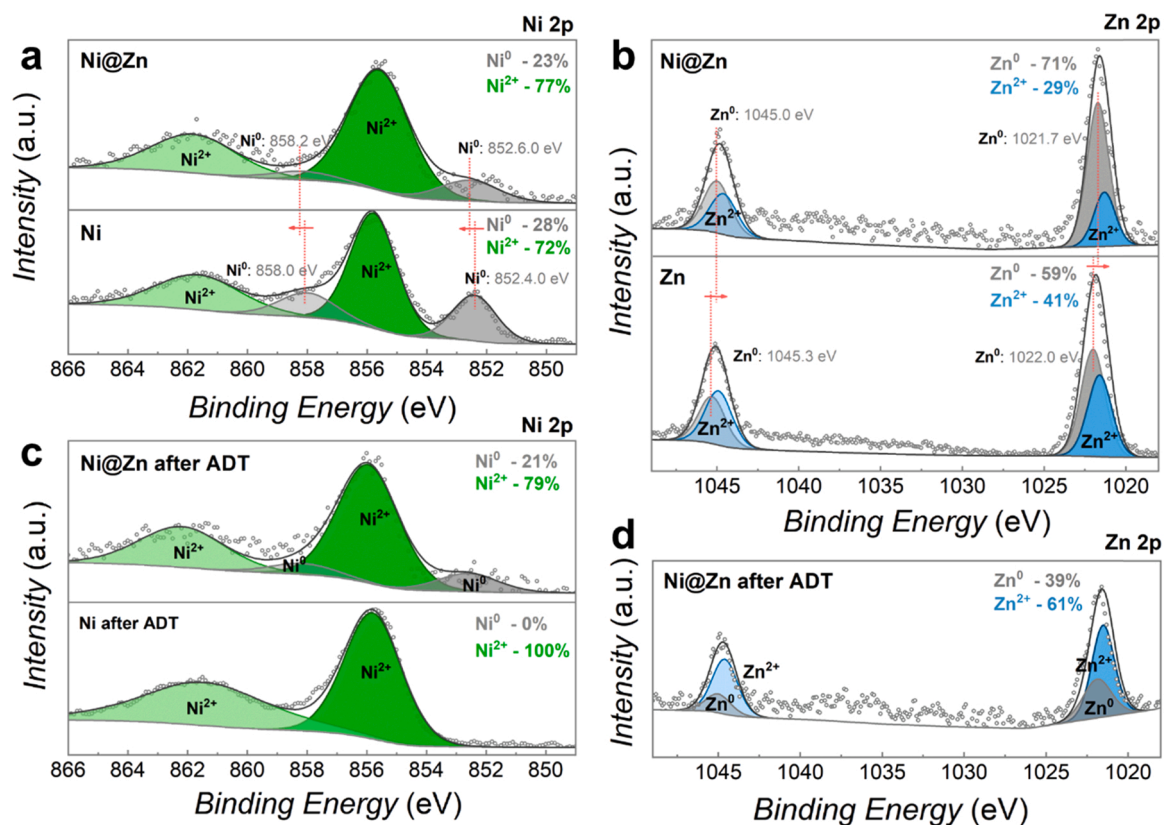


Fig. 3. X-ray photoelectron (a,c) Ni 2p<sub>3/2</sub> and (b,d) Zn 2p<sub>3/2</sub> spectra obtained for Ni@Zn, Ni and Zn samples before (a,b) and after (c,d) ADT.

The chemical states of the catalysts' surface characterized by X-ray photoelectron spectroscopy (XPS) are shown in Fig. 3. Two peaks centered at ca. 855.7 eV and 861.4 eV are assigned to Ni oxide species and its satellite peak, respectively [49], due to the ex-situ measurement. While the characteristic peaks at ca. 852.4 eV and 858.0 eV are confirmed to  $\text{Ni}^0$  and its satellite peak [50]. It can be found that the binding energy (BE) of  $\text{Ni}^0$  in  $\text{Ni@Zn}$  is higher than in Ni. Concerning Zn 2p level spectra, the peaks at ca. 1021.3 eV and 1044.6 eV represent oxidized Zn species originating from inevitable exposure in the air as well, and the  $\text{Zn}^0$  can correspond to peaks at ca. 1021.7 eV and its satellite peaks at ca. 1045.0 eV [51]. Contrary to the BE of  $\text{Ni}^0$ , the BE of  $\text{Zn}^0$  in  $\text{Ni@Zn}$  is lower than in Zn. The positive shift of BE of  $\text{Ni}^0$  and negative shift of BE of  $\text{Zn}^0$  indicate electrons deviate from Ni to Zn in the  $\text{Ni@Zn}$  catalyst. It may be attributed to the weaker attraction of Ni to extranuclear electrons owing to the less effective nuclear charge of Ni (3.7) than that of Zn (4.0). Moreover, the electron deviation from Ni to Zn in  $\text{Ni@Zn}$  is beneficial to promote catalytic reaction [52]. So, the introduction of Zn may change the charge distribution of Ni, which may be beneficial to enhance the catalytic activity to BOR. Certainly, the change of the electronic structure also proves that strong interaction exists between Ni shell and Zn core in  $\text{Ni@Zn}$  catalyst.

As mentioned before, the degree of Ni oxidation is crucial for the catalytic activity of Ni to BOR. To further explore the effect of Zn on the stability of  $\text{Ni@Zn}$ , the chemical states of Ni and Zn after the accelerated durability test (ADT) are also evaluated by XPS. As shown in Fig. 3c, it can be found that after ADT, the  $\text{Ni}^0$  content of Ni catalyst is greatly reduced, confirming the metallic Ni does significantly oxidize during the BOR. Unlike Ni catalyst, however, the content of  $\text{Ni}^0$  in  $\text{Ni@Zn}$  maintains very well, while the content of  $\text{Zn}^0$  in  $\text{Ni@Zn}$  decreases after ADT. It can be reasonably inferred that Zn in  $\text{Ni@Zn}$  catalysts may be used as a

sacrificial metal and oxidized instead of Ni during the BOR process, thereby preventing Ni from passivation. This can be attributed to the fact that the oxidation potential of Zn is more negative than that of Ni (Fig. 4a). Therefore, the introduction of Zn can maintain effectively metallic Ni, which has a high activity to BOR, and consequently improve the stability of  $\text{Ni@Zn}$ .

Nevertheless, the oxidation of Zn may bring a new problem, that is, the disintegration of leaf-shaped frameworks. As shown in Fig. 4a, the black surface of the Zn electrode disappears and the bright NS substrate exposes after the linear sweep voltammetry (LSV) in an alkaline solution. This indicates that the Zn framework is oxidized, the amphoteric Zn oxide species (e.g.,  $\text{ZnO}$  and  $\text{Zn(OH)}_2$ ) are formed and dissolved in the strong alkaline electrolyte (Fig. 4b). The disintegration of the framework would destroy the hierarchical morphology and seriously reduce the activity of catalysts; thus, it is necessary to verify and eliminate this hidden danger in  $\text{Ni@Zn}$ .

The coverage layer of Ni may have a protective effect on the leaf-shaped framework due to the fact that no NS substrate exposure is observed on the surface of  $\text{Ni@Zn}$  electrode after ADT. To confirm this inference, the influence of deposition time of Ni on the structural stability of  $\text{Ni@Zn}$  was explored. The catalysts with different deposition times are represented by  $\text{Ni-}x\text{@Zn}$ , and  $x$  is the deposition time (s). From Fig. S6e, it can be found that the honeycomb arrays of  $\text{Ni-10@Zn}$  prepared under short deposition time have collapsed obviously after ADT. Moreover, in enlarging the collapsed area (Fig. 4c), the leaves wrapped incompletely are also observed. This phenomenon shows that the exposed frameworks, owing to the incomplete encapsulation under insufficient deposition time, are oxidized and dissolved in the process of BOR, leading to the hierarchical morphology collapse, as shown in Fig. 4d. When the deposition time is sufficient, leaf-shaped frameworks

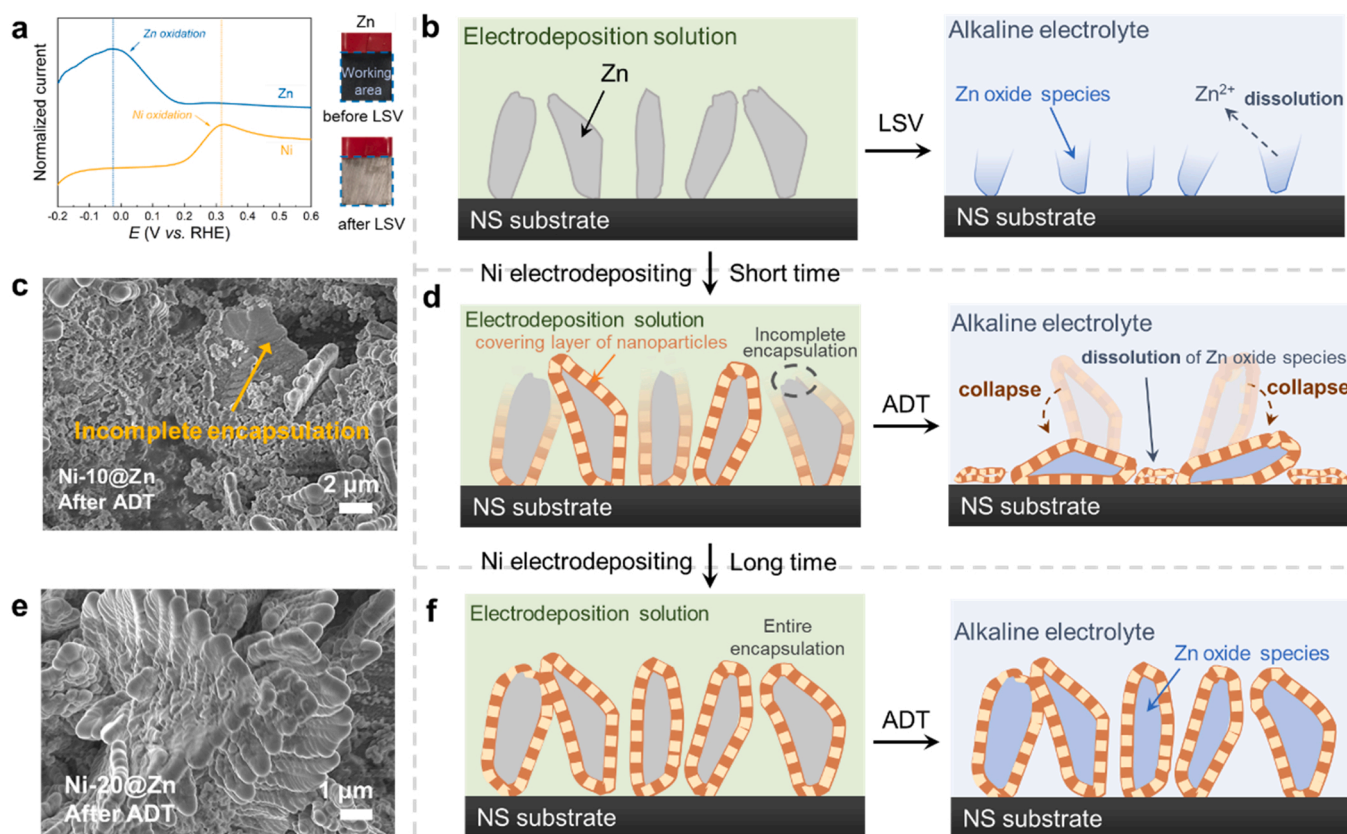


**Fig. 4.** (a) LSV curves of Zn and Ni on the left side, the digital photographs of Zn before and after LSV are on the right side (The peak at ca. -0.03 V vs. RHE in the case of Zn is ascribed to the oxidation of Zn and the peak at ca. 0.3 V vs. RHE is attributed to the formation of the higher valence of Ni surface oxygenates via reaction of Ni surface with  $\text{OH}^-$  in alkaline solution [53,54]); the enlarged SEM images of  $\text{Ni-10@Zn}$  (c) and  $\text{Ni-20@Zn}$  (e) after ADT; the schematic diagram of structural changes of (b) Zn, (d)  $\text{Ni-10@Zn}$ , and (f)  $\text{Ni-20@Zn}$  tested in the alkaline solution.

are completely wrapped (Fig. 4e) and the honeycomb arrays are intact after ADT (Fig. S6g). So, the coverage layer can act as a guard shelter to protect the leaf-shaped framework from dissolution and collapse, improving the structural stability of catalyst (Fig. 4f). In general, the sacrifice of Zn and the protection of Ni would together contribute to the improvement of Ni@Zn catalyst stability.

### 3.2. Electrocatalytic BOR performance

To attain the optimal performance of catalysts, then the electrochemical properties of BOR on Ni-x@Zn catalysts are systematically investigated. ECSA of Ni-x@Zn catalysts increases with the increases of deposition time from 10 to 20 s (Fig. 5a) followed by a significant drop when deposition time further increases to 30 s. It can be ascribed to the disappearance of multilayer leaves structure in Ni-30@Zn catalyst because the coverage layer of Ni grows too thick as excessive deposition time (Fig. S6d). Therefore, the performance of Ni-x@Zn catalysts is affected markedly by deposition time of Ni. LSV curves of BOR on Ni-x@Zn are demonstrated in Fig. 5b. The relationship curve between deposition time and activity of catalyst presents a volcano (Fig. 5c), which is consistent with the change rule of ECSA with deposition time. Among these catalysts, Ni-20@Zn yields the highest BOR activity with the current density of  $241 \text{ mA cm}^{-2}$  at  $0.3 \text{ V}$  vs. RHE. Moreover, oxidation peaks shift to a more positive potential with an increase of deposition time (Fig. 5c), which also indicates that the coverage layer wraps the framework more completely and better protection. As shown in Fig. 5d, Tafel slope for BOR increases with increasing deposition time, implying that the kinetic process of BOR proceeds more slowly when coverage layer thickens. The behavior of BOR on synthesized catalysts is evaluated by EIS in  $0.135 \text{ M NaBH}_4$  and  $2 \text{ M NaOH}$  mixture solution at  $E = 0.1 \text{ V}$  vs. RHE (Fig. 5e). On all catalysts, Nyquist plots show a semicircle, and obtained EIS data are fitted with the equivalent circuit shown in the insert of Fig. 5e, where  $R_s$  is the solution resistance, CPE is the constant phase element of interfacial double layer for electrode, and  $R_{ct}$  is charge transfer resistance [39].  $R_{ct}$  for Ni-x@Zn catalysts are summarized in Table S1. According to the results, a larger  $R_{ct}$  of BOR is

demonstrated on catalysts prepared under longer deposition time. This indicates the thickening of the Ni layer is not conducive to the mass transfer of charges, which is consistent with the results of Tafel slope. Meanwhile, BOR becomes harder to perform on Ni-x@Zn catalysts because  $E_a$  increases with the deposition time as well in Fig. 5f. This could be imputed to longer Ni deposition in Ni@Zn, as the greater proportion of Ni shown in Fig. S7 and Table S2, may weaken the regulation of Zn on Ni electronic structure, which is not conducive to strengthening the charge transport ability of BOR. Although the kinetic process of BOR on the Ni@Zn prepared at a short deposition time is fast, the structural stability of the catalyst is also a major consideration. Hence, there is a balance between catalytic activity and stability of Ni@Zn towards BOR. The win-win situation in terms of catalytic activity and stability can be achieved only when the Ni@Zn catalysts are prepared under an appropriate deposition time, that is 20 s

Next, the catalytic activity of different Ni-based catalysts, including Ni@Zn, NiZn, Ni, and NS catalysts, are compared. ECSA of Ni@Zn, NiZn, Ni, and NS is 134, 84, 85, and  $24 \text{ cm}^2$ , respectively (Fig. 6a). The morphology of Ni@Zn catalyst is different from NiZn, and Ni catalysts (see Fig. S9). So, the maximum ECSA of Ni@Zn benefits from its unique hierarchical morphology, which can provide an abundant amount of available reactive sites for BOR. Fig. S10 provides LSV curves of BOR in  $0.135 \text{ M NaBH}_4$  and  $2 \text{ M NaOH}$  solution on the Ni@Zn, NiZn, Ni, and NS, respectively. Remarkably higher BOR current density ( $241 \text{ mA cm}^{-2}$ ) at  $E = 0.3 \text{ V}$  vs. RHE is obtained on Ni@Zn catalyst than on others, indicating its much better catalytic activity towards BOR. Moreover, on Ni@Zn, BOR also has the highest ECSA-normalized current density ( $j_{\text{ECSA}}$ ). It implies Ni@Zn possesses the highest intrinsic activity to BOR, which can be ascribed to the change of crystal plane orientation and electron distribution by the introduction of Zn. From Fig. 6b and Table S3, on Ni@Zn, BOR exhibits the highest current density at  $E = 0.3 \text{ V}$  vs. RHE, indicating outstanding catalytic activity. Besides, it can be seen from Fig. 6c that, when the current density is  $10 \text{ mA cm}^{-2}$ , the overpotential of BOR on Ni@Zn is much lower than on NiZn, Ni, and NS, indicating that Ni@Zn has the highest activity to BOR as well. These can be attributed to its much larger ECSA providing a

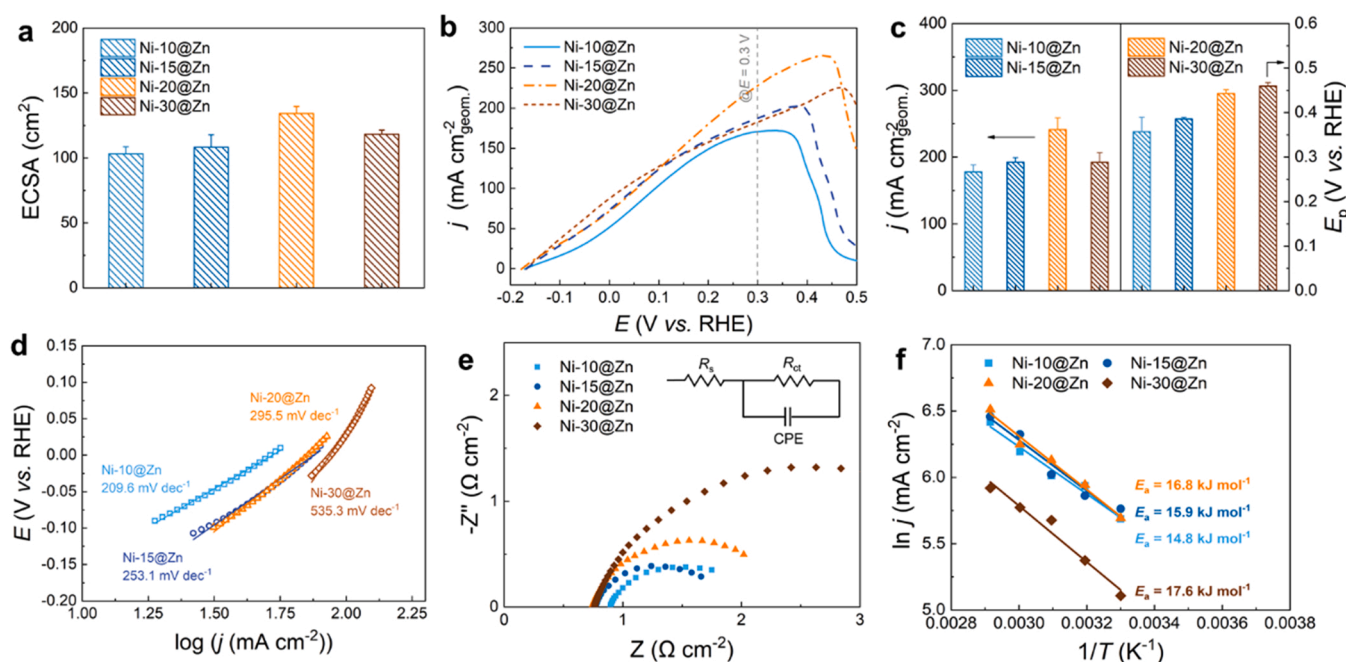


**Fig. 5.** (a) ECSAs of the Ni-x@Zn catalysts; (b) LSV curves of BOR on the Ni-x@Zn catalysts in  $0.135 \text{ M NaBH}_4$  and  $2 \text{ M NaOH}$  solution (scan rate of  $10 \text{ mV s}^{-1}$  at  $298 \text{ K}$ ); (c) current densities (@  $E = 0.3 \text{ V}$  vs. RHE) and  $E_p$  of BOR on Ni-x@Zn catalysts; (d) the corresponding Tafel slopes fitted based on the results in (b); (e) EIS curves for Ni-x@Zn catalysts in  $0.135 \text{ M NaBH}_4$  and  $2 \text{ M NaOH}$  solution at  $0.1 \text{ V}$  vs. RHE (insert is the equivalent circuit); (f) Arrhenius plots of BOR on Ni-x@Zn catalysts at  $0.3 \text{ V}$  vs. RHE (scan rate of  $10 \text{ mV s}^{-1}$ ) based on the results in Fig. S8.



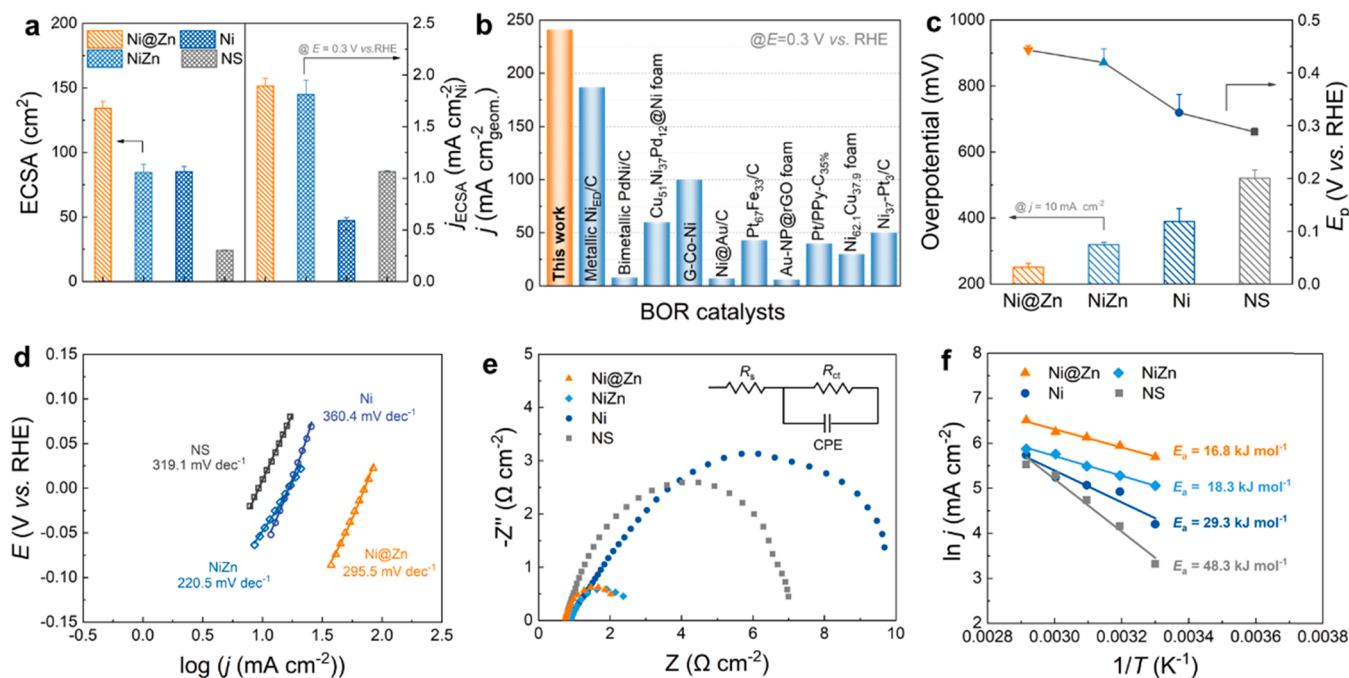


**Fig. 6.** (a) ECSA of different catalysts and the ECSA-normalized current densities of BOR on different catalysts at  $E = 0.3$  V vs. RHE; (b) current densities of BOR on Ni@Zn and catalysts reported previously (Table S3); (c) corresponding the overpotential required at  $j = 10$  mA cm⁻² and  $E_p$ ; (d) the corresponding Tafel slopes fitted based on the results in Fig. S10; (e) EIS curves for Ni@Zn, NiZn, Ni, and NS catalysts in 0.135 M NaBH<sub>4</sub> and 2 M NaOH solution at 0.1 V vs. RHE (insert is the equivalent circuit); (f) Arrhenius plots of BOR on Ni@Zn, NiZn, Ni, and NS catalysts at 0.3 V vs. RHE (scan rate of 10 mV s⁻¹) based on the results in Fig. S8.

mass of available reactive sites for BOR and a preferred orientation of the (220) crystal facet contributing to the bond breaking of BH<sub>4</sub><sup>-</sup> [48,55]. In addition, it can be found in Fig. S10 that on the Ni and NS, the current density is falling fast at about 0.3 V vs. RHE. It may be because the activities of these two catalysts decrease markedly both due to the oxidation Ni generated in this situation [12]. Whereas the peaks of Ni@Zn and NiZn shift to more positive potentials (Fig. 6c and Fig. S10). As mentioned above, the introduction of Zn is beneficial to inhibition of passivation of Ni catalysts owing to easiness of Zn oxidation.

The kinetics of BOR on different catalysts were evaluated by Tafel slope. BOR exhibits much lower Tafel slopes both on Ni@Zn and NiZn catalysts than on Ni and NS catalysts (Fig. 6d), which suggests that the introduction of Zn can also speed up the kinetics of BOR. Besides, EIS was also conducted to study the catalytic kinetics. From Fig. 6e, Ni@Zn displays the lowest  $R_{ct}$ , indicating the BOR is much easier to perform on Ni@Zn than on other Ni-based catalysts, which is in accord with the activity studies. Additionally, the lowest value of  $E_a$ , which is 16.8 kJ mol⁻¹, obtained on Ni@Zn implies that BOR is easiest to occur on it due to its unique hierarchical morphology and strong interaction of Ni and Zn. These can be attributed to the strong interaction between Ni and Zn according to the XPS.

The catalyst's selectivity to BOR was also investigated. The ECSA normalized exchange current density ( $j_0$ -ECSA) of HER is used to evaluate the intrinsic activity of the catalyst to competing HER.  $j_0$ -ECSA is obtained by the epitaxy method corresponding to the Tafel curves in Fig. S11a. From Fig. 7a, much lower  $j_0$ -ECSA is measured on Ni@Zn than on Ni, indicating that the catalytic sites of Ni@Zn have a lower activity to HER than that of Ni. The better selectivity of Ni@Zn to BOR may be attributed to the introduction of Zn as well. Since Zn exhibits a much higher overpotential of HER, compared with Ni (Fig. S11b). The interaction between Ni and Zn may reduce the activity of Ni@Zn catalyst to HER, which is also verified on NiZn catalyst.

In order to determine fuel efficiency on catalysts, a chronopotentiometry (CP) measurement was performed at a current density of 10 mA cm⁻² in 0.135 M NaBH<sub>4</sub> and 2 M NaOH solution. As shown in Fig. 7a, the highest fuel efficiency of NaBH<sub>4</sub> is obtained on Ni@Zn, being

ca. 1.2 times and 1.6 times higher than that on Ni and NiZn, respectively. It should be noted that there is not a direct anticorrelation between the activity towards HER and the fuel efficiency of NaBH<sub>4</sub> on these catalysts. Because fuel efficiency measurement is a long-term process, except for HER activity evaluation, certain factors also have much influence on fuel efficiency, for instance, the ability to capture and further oxidize escaped H<sub>2</sub>, and the stability catalyst. For Ni@Zn, first and foremost, the unique hierarchical morphology originating from stacking multilayer leaves could hinder the escape of H<sub>2</sub> generated by the hydrolysis of BH<sub>4</sub><sup>-</sup> and HER. Moreover, the high degree of preferred orientation of (220) crystal facet with a high specific surface energy of Ni@Zn can strengthen the adsorption to escaping H<sub>2</sub> [48]. Thus, Ni@Zn could capture more H<sub>2</sub> than other Ni-based catalysts and make it further oxidize, which is illustrated in Fig. 7c. Also, the core-shell structure of Ni@Zn could provide a guarantee for the stable existence of Zn and ensure the high catalytic selectivity to BOR during the long-term test. However, Zn in NiZn catalyst cannot be protected, thus, the high selectivity and stability of catalyst would be lost in the long-term test, resulting in lower fuel efficiency.

ADT was performed on Ni@Zn catalyst to estimate its stability. As shown in Fig. 7d, LSV curves of BOR before and after 500 cycles of CVs coincide basically on Ni@Zn catalyst. Besides, the morphology of Ni@Zn catalyst also remains intact after 500 cycles of CVs according to Fig. S6g. The preferred orientation degree of each crystal facet of Ni@Zn catalyst remains almost unchanged after CA test at different potentials (Fig. S12a and b). Similarly, the ECSA of Ni@Zn after ADT is 137 cm² (Fig. S12c) quite close to that before ADT (134 cm²). These indicate its robustness is excellent. Additionally, it is impressive that Ni@Zn also exhibits extraordinary stability in the long-term test in Fig. 7e. The current density of BH<sub>4</sub><sup>-</sup> oxidation on Ni@Zn catalyst decreases due to concentration attenuation of BH<sub>4</sub><sup>-</sup> during BOR processes. After replacing the new electrolyte, the current density of BOR on Ni@Zn catalyst drops slightly, and the current retention is still 92% after discharging for 50 h. Besides, the crystal structure of Ni@Zn also remains unchanged after the long-term CA test shown in Fig. S12d. High stability of Ni@Zn catalyst is attributed to the fact that Zn maintains the metallicity of Ni, and the

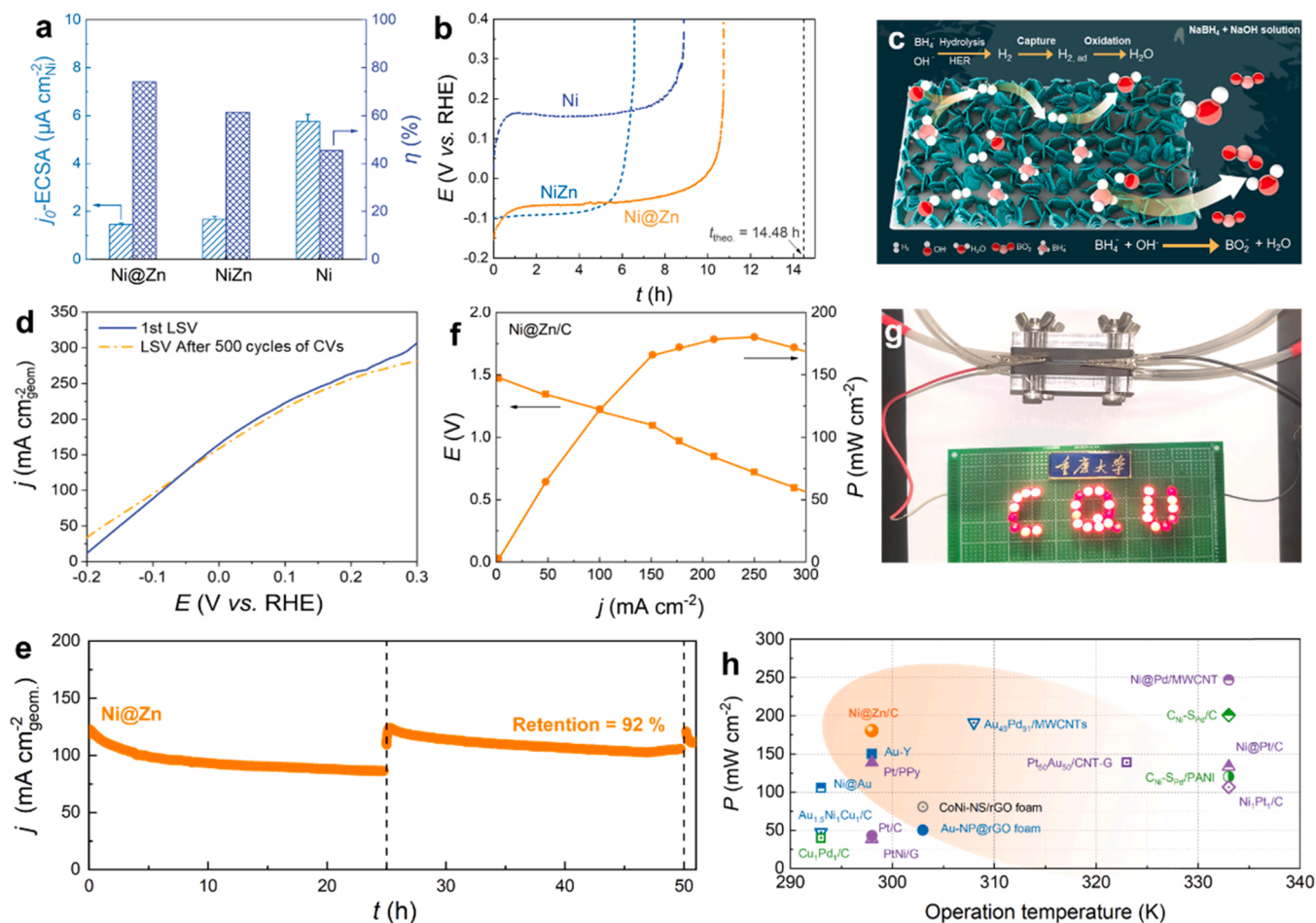


**Fig. 7.** (a)  $j_0$ -ECSA of HER and fuel efficiency on different catalysts; (b) discharge curves of  $\text{BH}_4^-$  on Ni@Zn, NiZn, and Ni catalysts in 0.135 M NaBH<sub>4</sub> and 2 M NaOH solution at a current density of 10 mA cm<sup>-2</sup> and 298 K; (c) Schematic diagram of reaction process on Ni@Zn; (d) The ADT for Ni@Zn; (e) long-term stability test of Ni@Zn catalyst; (f) I-E and I-P curves of DBFC with Ni@Zn/C anode, Pt/C cathode, 1 M NaBH<sub>4</sub> and 3 M NaOH anolyte and 4 M H<sub>2</sub>O<sub>2</sub> and 1 M H<sub>2</sub>SO<sub>4</sub> catholyte; (g) an application of DBFC to light a series of bulbs; (h) Performance comparison of some DBFCs with different anode catalysts (Table S4).

coverage layer of Ni on frameworks ensures the structural stability.

A unit DBFC, which is assembled by Ni@Zn/C catalyst as the anode and 1 M NaBH<sub>4</sub> and 3 M NaOH mixture solution as anolyte, Pt/C as the cathode and 4 M H<sub>2</sub>O<sub>2</sub> and 1 M H<sub>2</sub>SO<sub>4</sub> mixture solution as catholyte, and Nafion 117 as the membrane, is implemented to further evaluate the catalytic performance of catalysts. The DBFC obtains a peak power density of 180.3 mW cm<sup>-2</sup> at 298 K shown in Fig. 7 f. Fig. 7 g exhibits that an assembled DBFC can light up a series of small bulbs, which demonstrates thoroughly the practically applied prospect of Ni@Zn catalyst in DBFC. According to Fig. 7 h and Table S4, when Ni@Zn/C is used as the anode catalyst of DBFC, high power density can be achieved at 298 K. This indicates that Ni@Zn/C is a more promising anode catalyst of DBFC in practical applications. These results prove the hierarchical morphology and interaction between Ni and Zn in Ni@Zn anode catalyst can significantly improve the performances of DBFC.

#### 4. Conclusion

In summary, a facile strategy for the synthesis of efficient Ni@Zn catalyst with hierarchical morphology is presented. The unique hierarchical morphology composes of honeycomb-array by the leaves with Ni shell and Zn core structure stacking. Compared with other catalysts, the BOR on the Ni@Zn catalyst exhibits the lowest overpotential (250 mV at 10 mA cm<sup>-2</sup>), and the highest current density of 241 mA cm<sup>-2</sup>. The metallic Ni content and catalytic activity of Ni@Zn also remain unchanged after 500 cycles of CVs. On Ni@Zn, the utilization rate of  $\text{BH}_4^-$

can reach 74.2%, much better than that on other Ni-based catalysts. Besides, DBFC can export the peak power density of 180.3 mW cm<sup>-2</sup> when using Ni@Zn/C catalyst as the anode at 298 K. All these excellent performances are attributed to the synergy of the unique hierarchical morphology and the introduction of Zn into the catalyst. This study may pave a new path to design and develop noble-metal-free catalysts with low-cost, unique morphology, and high activity, stability, and selectivity for DBFC.

#### CRediT authorship contribution statement

**Bihao Hu:** Data curation, Writing – original draft, Visualization, Conceptualization. **Peng Chen:** Conceptualization, Investigation, Methodology. **Chuanlan Xu:** Writing – review & editing, Data curation. **Jiazhi Meng:** Visualization, Resources. **Jinliang Cai:** Validation, Writing – review. **Ying Yang:** Validation. **Biao Zhang:** Validation. **Danmei Yu\*:** Writing – review & editing, Supervision. **Xiaoyuan Zhou\*:** Resources. **Changguo Chen\*:** Funding acquisition.

#### Declaration of Competing Interest

The authors declare that they have no known competing financial interests or personal relationships that could have appeared to influence the work reported in this paper.



## Acknowledgments

This work is supported by the National Natural Science Foundation of China (No. 21273292, No. 21406021). We would like to thank Dr. Bin Zhang et al. from the Analytic and Testing Center of Chongqing University for their help in the characterization of material properties.

## Appendix A. Supporting information

Supplementary data associated with this article can be found in the online version at [doi:10.1016/j.apcatb.2022.121183](https://doi.org/10.1016/j.apcatb.2022.121183).

## References

- J.P. Elder, A. Hickling, Anodic behaviour of the borohydride ion, *Trans. Faraday Soc.* 58 (1962) 1852–1864, <https://doi.org/10.1039/tf9625801852>.
- G.H. Miley, N. Luo, J. Mather, R. Burton, G. Hawkins, L. Gu, E. Byrd, R. Gimlin, P. J. Shrestha, G. Benavides, J. Laystrom, D. Carroll, Direct  $\text{NaBH}_4/\text{H}_2\text{O}_2$  fuel cells, *J. Power Sources* 165 (2007) 509–516, <https://doi.org/10.1016/j.jpowsour.2006.10.062>.
- J.I. Martins, M.C. Nunes, R. Koch, L. Martins, M. Bazzou, Electrochemical oxidation of borohydride on platinum electrodes: the influence of thiourea in direct fuel cells, *Electrochim. Acta* 52 (2007) 6443–6449, <https://doi.org/10.1016/j.electacta.2007.04.066>.
- J.H. Wee, Which type of fuel cell is more competitive for portable application: direct methanol fuel cells or direct borohydride fuel cells? *J. Power Sources* 161 (2006) 1–10, <https://doi.org/10.1016/j.jpowsour.2006.07.032>.
- I. Merino-Jiménez, C. Ponce De León, A.A. Shah, F.C. Walsh, Developments in direct borohydride fuel cells and remaining challenges, *J. Power Sources* 219 (2012) 339–357, <https://doi.org/10.1016/j.jpowsour.2012.06.091>.
- Y. Kojima, T. Haga, Recycling process of sodium metaborate to sodium borohydride, *Int. J. Hydrog. Energy* 28 (2003) 989–993, [https://doi.org/10.1016/S0360-3199\(02\)00173-8](https://doi.org/10.1016/S0360-3199(02)00173-8).
- C.P. de Leon, F.C. Walsh, D. Pletcher, D.J. Browning, J.B. Lakeman, Direct borohydride fuel cells, *J. Power Sources* 155 (2006) 172–181, <https://doi.org/10.1016/j.jpowsour.2006.01.011>.
- L. Gu, N. Luo, G.H. Miley, Cathode electrocatalyst selection and deposition for a direct borohydride/hydrogen peroxide fuel cell, *J. Power Sources* 173 (2007) 77–85, <https://doi.org/10.1016/j.jpowsour.2007.05.005>.
- M. Chatenet, Tailoring membranes, *Nat. Energy* 4 (2019) 261–262, <https://doi.org/10.1038/s41560-019-0348-8>.
- C.P. de León, F.C. Walsh, A. Rose, J.B. Lakeman, D.J. Browning, R.W. Reeve, A direct borohydride-Acid peroxide fuel cell, *J. Power Sources* 164 (2007) 441–448, <https://doi.org/10.1016/j.jpowsour.2006.10.069>.
- C. Grimmer, M. Grandi, R. Zacharias, B. Cermenek, H. Weber, C. Morais, T. W. Napporn, S. Weinberger, A. Schenk, V. Hacker, The electrooxidation of borohydride: a mechanistic study on palladium (Pd/C) applying RRDE,  $^{11}\text{B}$  NMR and FTIR, *Appl. Catal. B Environ.* 180 (2016) 614–621, <https://doi.org/10.1016/j.apcatb.2015.07.028>.
- A.G. Oshchepkov, G. Braesch, S. Ould-Amara, G. Rostamikia, G. Maranzana, A. Bonnefont, V. Papaefthimiou, M.J. Janik, M. Chatenet, E.R. Savinova, Nickel Metal nanoparticles as anode electrocatalysts for highly efficient direct borohydride fuel cells, *ACS Catal.* 9 (2019) 8520–8528, <https://doi.org/10.1021/acscatal.9b01616>.
- P.C.K. Vesborg, T.F. Jaramillo, Addressing the terawatt challenge: scalability in the supply of chemical elements for renewable energy, *RSC Adv.* 2 (2012) 7933–7947, <https://doi.org/10.1039/c2ra20839c>.
- P.Y. Olu, N. Job, M. Chatenet, Evaluation of anode (electro)catalytic materials for the direct borohydride fuel cell: methods and benchmarks, *J. Power Sources* 327 (2016) 235–257, <https://doi.org/10.1016/j.jpowsour.2016.07.041>.
- P.Y. Olu, F. Deschamps, G. Caldarella, M. Chatenet, N. Job, Investigation of platinum and palladium as potential anodic catalysts for direct borohydride and ammonia borane fuel cells, *J. Power Sources* 297 (2015) 492–503, <https://doi.org/10.1016/j.jpowsour.2015.08.022>.
- M. Shao, Palladium-based electrocatalysts for hydrogen oxidation and oxygen reduction reactions, *J. Power Sources* 196 (2011) 2433–2444, <https://doi.org/10.1016/j.jpowsour.2010.10.093>.
- M. Simoes, S. Baranton, C. Coutanceau, Electrooxidation of sodium borohydride at Pd, Au, and  $\text{Pd}_x\text{Au}_{1-x}$  carbon-supported nanocatalysts, *J. Phys. Chem. C* 113 (2009) 13369–13376, <https://doi.org/10.1021/jp902741z>.
- A.M. Pasqualetti, P.Y. Olu, M. Chatenet, F.H.B. Lima, Borohydride electrooxidation on carbon-supported noble metal nanoparticles: insights into hydrogen and hydroxyborane formation, *ACS Catal.* 5 (2015) 2778–2787, <https://doi.org/10.1021/acscatal.5b00107>.
- G. Braesch, Z. Wang, S. Sankarasubramanian, A.G. Oshchepkov, A. Bonnefont, E. R. Savinova, V. Ramani, M. Chatenet, A high performance direct borohydride fuel cell using bipolar interfaces and noble metal-free Ni-based anodes, *J. Mater. Chem. A* 8 (2020) 20543–20552, <https://doi.org/10.1039/d0ta06405j>.
- G. Braesch, A.G. Oshchepkov, A. Bonnefont, F. Asonkeng, T. Maurer, G. Maranzana, E.R. Savinova, M. Chatenet, Nickel 3D structures enhanced by electrodeposition of nickel nanoparticles as high performance anodes for direct borohydride fuel cells, *ChemElectroChem* 7 (2020) 1789–1799, <https://doi.org/10.1002/celec.202000254>.
- W. Ni, T. Wang, P.A. Schouwink, Y.C. Chuang, H.M. Chen, X. Hu, Efficient hydrogen oxidation catalyzed by strain-engineered nickel nanoparticles, *Angew. Chem. - Int. Ed.* 59 (2020) 10797–10801, <https://doi.org/10.1002/anie.201916314>.
- T. Wang, M. Wang, H. Yang, M. Xu, C. Zuo, K. Feng, M. Xie, J. Deng, J. Zhong, W. Zhou, T. Cheng, Y. Li, Weakening hydrogen adsorption on nickel via interstitial nitrogen doping promotes bifunctional hydrogen electrocatalysis in alkaline solution, *Energy Environ. Sci.* 12 (2019) 3522–3529, <https://doi.org/10.1039/c9ee01743g>.
- M. Gong, D.Y. Wang, C.C. Chen, B.J. Hwang, H. Dai, A mini review on nickel-based electrocatalysts for alkaline hydrogen evolution reaction, *Nano Res* 9 (2016) 28–46, <https://doi.org/10.1007/s12274-015-0965-x>.
- E. Gyenge, M. Atwan, D. Northwood, Electrocatalysis of borohydride oxidation on colloidal Pt and Pt-Alloys (Pt-Ir, Pt-Ni, and Pt-Au) and application for direct borohydride fuel cell anodes, *J. Electrochem. Soc.* 153 (2006) A150, <https://doi.org/10.1149/1.2131831>.
- Y. Duan, Z.Y. Yu, L. Yang, L.R. Zheng, C.T. Zhang, X.T. Yang, F.Y. Gao, X.L. Zhang, X. Yu, R. Liu, H.H. Ding, C. Gu, X.S. Zheng, L. Shi, J. Jiang, J.F. Zhu, M.R. Gao, S. H. Yu, Bimetallic nickel-molybdenum/tungsten nanoalloys for high-efficiency hydrogen oxidation catalysis in alkaline electrolytes, *Nat. Commun.* 11 (2020) 1–10, <https://doi.org/10.1038/s41467-020-18585-4>.
- J. Yu, Q. Li, Y. Li, C.Y. Xu, L. Zhen, V.P. Dravid, J. Wu, Ternary metal phosphide with triple-layered structure as a low-cost and efficient electrocatalyst for bifunctional water splitting, *Adv. Funct. Mater.* 26 (2016) 7644–7651, <https://doi.org/10.1002/adfm.201603727>.
- J. Staszak-Jirkovský, C.D. Malliakas, P.P. Lopes, N. Danilovic, S.S. Kota, K. C. Chang, B. Genorio, D. Strmcnik, V.R. Stamenkovic, M.G. Kanatzidis, N. M. Markovic, Design of active and stable Co-Mo-S<sub>x</sub> chalcogenides as pH-universal catalysts for the hydrogen evolution reaction, *Nat. Mater.* 15 (2016) 197–203, <https://doi.org/10.1038/nmat4481>.
- D. Li, H. Baydoun, C.N. Verani, S.L. Brock, Efficient water oxidation using CoMnP nanoparticles, *J. Am. Chem. Soc.* 138 (2016) 4006–4009, <https://doi.org/10.1021/jacs.6b01543>.
- J. Yu, B. Hu, C. Xu, J. Meng, S. Yang, Y. Li, X. Zhou, Y. Liu, D. Yu, C. Chen, Ni-P amorphous alloy efficient electrocatalyst with hierarchical structure toward borohydride oxidation, *Dalt. Trans.* (2021), <https://doi.org/10.1039/d1dt01031j>.
- R. Ghasemi, B.K. Moghadas, I. Mohammadi, Solvothermal synthesis of  $\text{Pd}_{10}\text{-Ni}_{45}\text{-Co}_{45}\text{-rGO}$  composites as novel electrocatalysts for enhancement of the performance of DBFC, *Int. J. Hydrog. Energy* 45 (2020) 21808–21815, <https://doi.org/10.1016/j.ijhydene.2020.05.172>.
- M.W. Glasscott, A.D. Pendergast, S. Goines, A.R. Bishop, A.T. Hoang, C. Renault, J. E. Dick, Electrosynthesis of high-entropy metallic glass nanoparticles for designer, multi-functional electrocatalysis, *Nat. Commun.* 10 (2019), <https://doi.org/10.1038/s41467-019-10303-z>.
- S.G. Kwon, G. Krylova, P.J. Phillips, R.F. Klie, S. Chattopadhyay, T. Shibata, E. E. Bunel, Y. Liu, V.B. Prakapenka, B. Lee, E.V. Shevchenko, Heterogeneous nucleation and shape transformation of multi-component metallic nanostructures, *Nat. Mater.* 14 (2015) 215–223, <https://doi.org/10.1038/nmat4115>.
- Y. Yao, Z. Huang, P. Xie, S.D. Lacey, R.J. Jacob, H. Xie, F. Chen, A. Nie, T. Pu, M. Rehwaldt, D. Yu, M.R. Zachariah, C. Wang, R. Shahbazian-Yassar, J. Li, L. Hu, Carbothermal shock synthesis of high-entropy-alloy nanoparticles, *Sci. (80-. )* 359 (2018) 1489–1494, <https://doi.org/10.1126/science.aan5412>.
- J. Wang, J. Zhou, J. Yang, D. Neagu, L. Fu, Z. Lian, T.H. Shin, K. Wu, Tailoring the surface of perovskite through in situ growth of Ru/RuO<sub>2</sub> nanoparticles as robust symmetrical electrodes for reversible solid oxide cells, *Adv. Mater. Interfaces* 7 (2020) 1–27, <https://doi.org/10.1002/admi.202000828>.
- K.C. Pingali, S. Deng, D.A. Rockstraw, Synthesis and thermal stability of carbon-supported Ru-Ni core-and-shell nanoparticles, *Powder Technol.* 187 (2008) 19–26, <https://doi.org/10.1016/j.powtec.2007.12.018>.
- R. Huang, Y.H. Wen, G.F. Shao, S.G. Sun, Insight into the melting behavior of Au-Pt core-shell nanoparticles from atomistic simulations, *J. Phys. Chem. C* 117 (2013) 4278–4286, <https://doi.org/10.1021/jp312048k>.
- N.M. Masaharu Tsuji, Ryoichi Matsuo, Peng Jiang, H.K. Daisuke Ueyama, Michiko Nishio, Sachie Hikino, X.-L.T. Khairul Sozana Nor Kamarudin, Shape-Dependent evolution of Au@Ag core - shell nanocrystals by & DESIGN 2008, *Cryst. Growth Des.* 8 (2008) 2528–2536.
- D. Duan, J. Liang, H. Liu, X. You, H. Wei, G. Wei, S. Liu, The effective carbon supported core-shell structure of Ni@Au catalysts for electro-oxidation of borohydride, *Int. J. Hydrog. Energy* 40 (2015) 488–500, <https://doi.org/10.1016/j.ijhydene.2014.10.101>.
- R. Mahmoodi, M.G. Hosseini, H. Rasouli, Enhancement of output power density and performance of direct borohydride-hydrogen peroxide fuel cell using Ni-Pd core-shell nanoparticles on polymeric composite supports (rGO-PANI) as novel electrocatalysts, *Appl. Catal. B Environ.* 251 (2019) 37–48, <https://doi.org/10.1016/j.apcatb.2019.03.064>.
- M.G. Hosseini, R. Mahmoodi, Improvement of energy conversion efficiency and power generation in direct borohydride-hydrogen peroxide fuel cell: the effect of Ni-M core-shell nanoparticles (M = Pt, Pd, Ru)/multiwalled carbon nanotubes on the cell performance, *J. Power Sources* 370 (2017) 87–97, <https://doi.org/10.1016/j.jpowsour.2017.10.017>.
- D. Duan, H. Liu, X. You, H. Wei, S. Liu, Anodic behavior of carbon supported Cu@Ag core-shell nanocatalysts in direct borohydride fuel cells, *J. Power Sources* 293 (2015) 292–300, <https://doi.org/10.1016/j.jpowsour.2015.05.086>.

- [42] Y.J. Han, X. Zhang, G.W. Leach, Shape control of electrodeposited copper films and nanostructures through additive effects, *Langmuir* 30 (2014) 3589–3598, <https://doi.org/10.1021/la500001j>.
- [43] S.A.S. Machado, L.A. Avaca, The hydrogen evolution reaction on nickel surfaces stabilized by H-absorption, *Electrochim. Acta* 39 (1994) 1385–1391, [https://doi.org/10.1016/0013-4686\(94\)E0003-1](https://doi.org/10.1016/0013-4686(94)E0003-1).
- [44] B. Li, C. Song, X. Huang, K. Ye, K. Cheng, K. Zhu, J. Yan, D. Cao, G. Wang, A novel anode for direct borohydride-hydrogen peroxide fuel Cell: Au Nanoparticles decorated 3D self-supported reduced graphene oxide foam, *ACS Sustain. Chem. Eng.* 7 (2019) 11129–11137, <https://doi.org/10.1021/acssuschemeng.9b00192>.
- [45] C. Xiao, B.A. Lu, P. Xue, N. Tian, Z.Y. Zhou, X. Lin, W.F. Lin, S.G. Sun, High-index-facet- and high-surface-energy nanocrystals of metals and metal oxides as highly efficient catalysts, *Joule* 4 (2020) 2562–2598, <https://doi.org/10.1016/j.joule.2020.10.002>.
- [46] T.V.W. Janssens, B.S. Clausen, B. Hvolbæk, H. Falsig, C.H. Christensen, T. Bligaard, J.K. Nørskov, Insights into the reactivity of supported Au nanoparticles: combining theory and experiments, *Top. Catal.* 44 (2007) 15–26, <https://doi.org/10.1007/s11244-007-0335-3>.
- [47] S.L. Bernasek, G.A. Somorjai, Small molecule reactions on stepped single crystal platinum surfaces, *Surf. Sci.* 48 (1975) 204–213, [https://doi.org/10.1016/0039-6028\(75\)90317-9](https://doi.org/10.1016/0039-6028(75)90317-9).
- [48] B. Hu, C. Xu, P. Chen, J. Yu, B. Hu, Q. Xiang, Y. Cen, Y. Liu, D. Yu, C. Chen, Efficient nickel catalyst with preferred orientation and microsphere for direct borohydride fuel cell, *Int. J. Hydrog. Energy* 46 (2021) 27516–27528, <https://doi.org/10.1016/j.ijhydene.2021.06.002>.
- [49] Z. Huang, Z. Chen, Z. Chen, C. Lv, H. Meng, C. Zhang, Ni<sub>12</sub>P<sub>5</sub> nanoparticles as an efficient catalyst for hydrogen generation via electrolysis and photoelectrolysis, *ACS Nano* 8 (2014) 8121–8129, <https://doi.org/10.1021/nn5022204>.
- [50] A. Roustila, C. Severac, J. Chène, A. Percheron-Guégan, Hydrogen effects on the electronic and microstructural properties of Ce, Ni, and CeNi<sub>2</sub> intermetallic compound, *Surf. Sci.* 311 (1994) 33–44, [https://doi.org/10.1016/0039-6028\(94\)90478-2](https://doi.org/10.1016/0039-6028(94)90478-2).
- [51] F. Li, W. Li, J. Li, W. Xue, Y. Wang, X. Zhao, Investigation of supported Zn(OAc)<sub>2</sub> catalyst and its stability in N-phenyl carbamate synthesis, *Appl. Catal. A Gen.* 475 (2014) 355–362, <https://doi.org/10.1016/j.apcata.2014.01.008>.
- [52] Y. e Duan, S. Li, Q. Tan, Y. Chen, K. Zou, X. Dai, M. Bayati, B.B. Xu, L. Dala, T. X. Liu, Cobalt nickel boride nanocomposite as high-performance anode catalyst for direct borohydride fuel cell, *Int. J. Hydrog. Energy* 46 (2021) 15471–15481, <https://doi.org/10.1016/j.ijhydene.2021.02.064>.
- [53] W. Ni, A. Krammer, C.S. Hsu, H.M. Chen, A. Schüller, X. Hu, Ni<sub>3</sub>N as an active hydrogen oxidation reaction catalyst in alkaline medium, *Angew. Chem. - Int. Ed.* 58 (2019) 7445–7449, <https://doi.org/10.1002/anie.201902751>.
- [54] T.Y. Jeon, M. Watanabe, K. Miyatake, Carbon segregation-induced highly metallic Ni nanoparticles for electrocatalytic oxidation of hydrazine in alkaline media, *ACS Appl. Mater. Interfaces* 6 (2014) 18445–18449, <https://doi.org/10.1021/am5058635>.
- [55] C. Xu, P. Chen, B. Hu, Q. Xiang, Y. Cen, B. Hu, L. Liu, Y. Liu, D. Yu, C. Chen, Porous nickel electrodes with controlled texture for the hydrogen evolution reaction and sodium borohydride electrooxidation, *CrystEngComm* 22 (2020) 4228–4237, <https://doi.org/10.1039/d0ce00344a>.